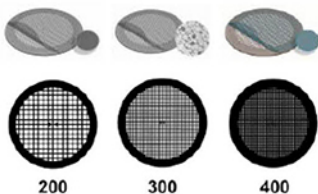# Nanocharacterization by TEM and AFM

We offer a wide range of TEM and AFM tools, from TEM grids and finders to AFM substrates and grippers.

Available in a wide variety of designs and materials to support your work, select from a broad range of mesh sizes, specimen supporting films, and materials that perfectly suit the conditions of your TEM analysis.

TEM grid specifications:

Material	Mesh Size and Shape	Film Specifications
• Cu • Ni • Au • Mo • Cu/Pd	• Square or hexagonal • Single-hole grid (75 mm or 100 mm) • 100 • 150 • 200 • 300 • 400	• None • Continuous formvar film (thicknesses: 5-6 nm, 10 nm) • Lacey carbon film (average hole sizes: 50 nm, 100 nm, 150 nm, 100 mm, 150 mm) • Continuous amorphous carbon film (thicknesses: 10 nm, 20-30 nm) • Continuous formvar/carbon film (thickness: 10nm formvar and 1nm carbon)

200   300   400

TEM finder grid specifications:

Material	Mesh Size	Film Specifications
• Cu • Ni • Au	• 135 • 200 • 300 • 400	• None • Continuous amorphous carbon film (thicknesses: 3-4 nm, 10 nm, 20-30 nm)
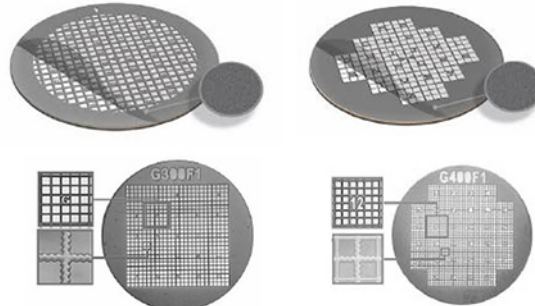
Supporting Tools for Nanomaterial Characterization

Our comprehensive range of supporting materials for nanomaterial characterization includes tweezers (sharp tip, disc gripper for AFM), TEM window grids (various thicknesses, 1 or 9 windows), a magnetic pick-up tool, a grid storage box, cryo-capsules, lift-out grids (Cu or Mo), AFM substrates (various dimensions), and much more.

Explore our complete range of TEM grids on:
SigmaAldrich.com/nanocharacterization

The Life Science business of Merck operates as MilliporeSigma in the U.S. and Canada.

Sigma-Aldrich®

Lab & Production Materials

Fast and Scalable Synthesis of LiNi$_{0.5}$Mn$_{1.5}$O$_4$ Cathode by Sol–Gel-Assisted Microwave Sintering

Umair Nisar, Sara Ahmad J. A. Al-Hail, Petla Ramesh Kumar, Jeffin James Abraham, Saoud M. A. Mesallam, Rana Abdul Shakoor,* Ruhul Amin,* Rachid Essehli, and Siham Al-Qaradawi

High-voltage spinel LiNi$_{0.5}$Mn$_{1.5}$O$_4$ (LNMO) is a promising cathode material for high-energy-density and high-power-density lithium-ion batteries (LIBs). The high cost of the currently available LIBs needs to be addressed urgently for wide application in the transport sector (electric vehicles, buses) and large-scale energy storage systems (ESS). Of significance, herein, novel fast and scalable microwave-assisted synthesis of LNMO is reported, which leads to a production cost cut. X-ray diffraction (XRD) analysis confirms the formation of the desired phase with high crystallinity. Field emission scanning (FE-SEM) and transmission electron microscopy (TEM) analyses indicate that the synthesized phase is of nanometric size (50–150 nm) due to an extremely short sintering time (20 min). The material synthesized at 750 °C shows a higher initial discharge capacity (130 mA h g^{-1}) than that synthesized at 650 °C (115 mA h g^{-1}). The materials heat treated at higher temperatures show better electrochemical performance in terms of initial capacity, rate capability, and improved cycling. The improved electrochemical performance of LNMO at 750 °C is attributed to the formation of a stable crystal structure, low charge transfer resistance at the electrode/electrolyte interface, high electrical conductivity due to the presence of a disorder structure, and improved ionic diffusivity.

1. Introduction

Lithium-ion batteries currently power almost all electronic devices and power tools; they are considered a key technology of choice for electric vehicles (EV) as well as for grid storage.[1–3] The demand for rechargeable lithium-ion batteries is exponentially increasing due to environmental consciousness and the effective use of renewable energy sources and EV applications.[1,2,4,5] In line with the diverse applicability, there is also an increase in the development and incorporation of innovative techniques for the design and cost-effective synthesis of electrode materials that lead to a diverse range of performance characteristics and fulfill the future energy demands of the growing society.[6–14] Therefore, in the quest to develop high-performance and cost-effective lithium-ion batteries, several different types of cathode materials have been developed and commercialized, including LiMn$_2$O$_4$, LiNi$_{0.5}$Mn$_{1.5}$O$_4$ (LNMO), LiNi$_{1/3}$Co$_{1/3}$Mn$_{1/3}$O$_2$, LiNi$_{0.5}$Co$_{0.2}$Mn$_{0.3}$O$_2$, LiNi$_{0.6}$Co$_{0.2}$Mn$_{0.2}$O$_2$, LiNi$_{0.8}$Co$_{0.15}$Al$_{0.05}$O$_2$, and LiFePO$_4$.[8,13,15,16] However, the issues related to safety and cost remain great challenges for future LIBs.[13,17,18–25,26] These issues are crucial for developing large-scale batteries for energy storage systems (ESS) and electric vehicles. Till the present, lithium-ion battery technology is also one of the most expensive amongst other battery technologies; therefore, to fulfill the demands for the transport sector and large-scale ESS,

U. Nisar, J. J. Abraham, Dr. R. A. Shakoor
Center for Advanced Materials (CAM)
Qatar University
P.O. Box 2713, Doha, Qatar
E-mail: shakoor@qu.edu.qa

S. A. J. A. Al-Hail, Dr. P. R. Kumar
Qatar Environment and Energy Research Institute
Hamad Bin Khalifa University
Qatar Foundation
34110 Doha, Qatar

S. M. A. Mesallam
Department of Mechanical Engineering
College of Engineering
Qatar University
P.O. Box 2713, Doha, Qatar

Dr. R. Amin, Dr. R. Essehli
Energy and Transportation Science Division
Oak Ridge National Laboratory
Oak Ridge 37830, TN, USA
E-mail: aminr@ornl.gov

Prof. S. Al-Qaradawi
Department of Chemistry & Earth Sciences
College of Arts and Science
Qatar University
P.O. Box 2713, Doha, Qatar

ADVANCED
SCIENCE NEWS
www.advancedsciencenews.com

Energy Technology
Generation, Conversion, Storage, Distribution
www.entechnol.de

the cost of LIBs needs to be decreased on priority.[7,13,27–34] One way to reduce the price of currently available lithium-ion battery technology is to minimize the cost of cathode and anode materials as they constitute a significant portion of the overall battery price.[35–37] There are also several other ways to decrease the price of currently available lithium-ion battery technology: 1) use of cheaper raw materials, 2) development of new materials with low cost, 3) fabrication of high-energy-density batteries, 4) decrease of the material production cost, and 5) lowering the battery manufacturing costs.[7,8,13,38,39] In addition to the aforementioned factors, we think, the material cost can also be decreased to a certain extent using cost-effective synthesis methods.

Till the present, many synthesis methods have been developed to prepare electrode materials, which include sol–gel, solid-state, coprecipitation, spray pyrolysis, and molten salt methods.[40–46] In these processes, the precursor has to be calcinated for about 8–12 h at high temperature, which greatly increases the production cost of these materials. Logically, reducing the synthesis temperature and time can contribute significantly to lowering the production cost of the electrode materials and thus the overall battery cost as these materials expressively share the overall cost of the battery pack. Microwave sintering is a relatively new synthesis approach where the synthesis time is extremely low due to its unique heating mechanism.[47,48] Unfortunately, not many reports are available so far for the synthesis of electrode materials using the microwave sintering approach.[49–54] The typical microwave sintering cycle operates at a relatively low sintering temperature and consumes only around 10–20 min of dwell time, which is extremely low compared to the conventional sintering approaches ($\approx$8–12 h). However, the major challenge is the synthesis of the impurity-free phase. Nonetheless, with proper understanding and engineering of the process, this technique can play a vital role in the cost-effective synthesis of electrode materials for a battery technology with better electrochemical performance.

In this study, the novel microwave-assisted sintering approach was used to synthesize high-voltage spinel LNMO and the effect of the synthesis temperature on the electrochemical performance was studied. Microwave sintering involves an extremely short sintering time (<20 min), which results in nanosized particles due to insufficient time for particle growth. The LNMO materials were synthesized at three different temperatures (650, 700, and 750 °C) for 20 min. After synthesis, the materials were characterized using various characterization tools such as X-ray diffraction (XRD), field emission scanning electron microscopy (FE-SEM), and transmission electron microscopy (TEM). The battery performance was evaluated through electrochemical charge/discharge, cycling, and electrochemical impedance spectroscopy (EIS).

2. Results and Discussion

The XRD patterns of synthesized LNMO materials are displayed in **Figure 1**a. The material D-700 (D stands for before decomposition) represents LNMO synthesized through direct microwave sintering at 700 °C for 20 min without decomposition of precursors before the microwave treatment. In contrast, P-650, P-700, and P-750 materials (P stands for pre-heat-treated) were synthesized by pre-heat treatment of precursors at 450 °C for 6 h and
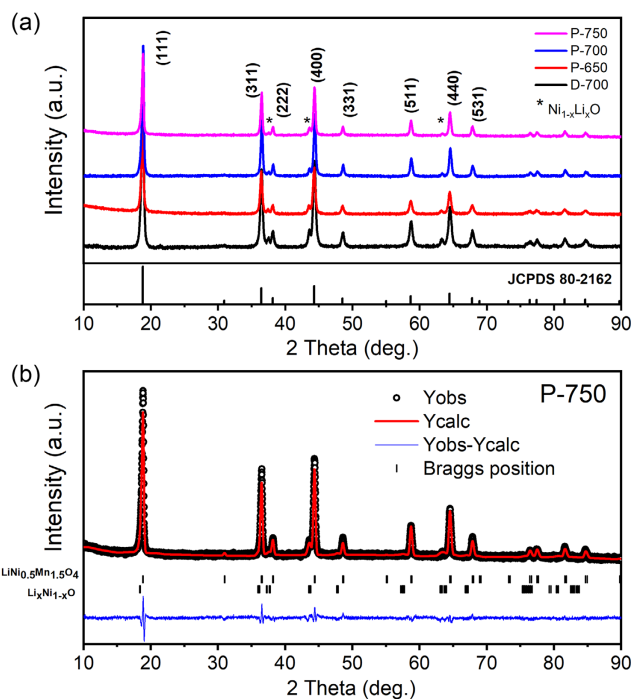

Figure 1. a) XRD patterns of D-700, P-650, P-700, and P-750 materials. b) Observed, calculated, and difference plots for powder X-ray diffraction (Cu Kα radiation) Rietveld refinement of P-750 sample (R_p = 8.89, R_{wp} = 12.54).

later sintered at 650–750 °C using a microwave furnace for 20 min. Thermogravimetric analysis (TGA) analysis for the precursor LNMO material is displayed as Figure S1, Supporting Information, which clearly shows that the precursor is completely decomposed at around 300 °C. The XRD analysis confirms the presence of LNMO materials with a trace amount of $Ni_{1-x}Li_xO$. Ideally, the general chemical formula for the spinel and rock salt oxides would be AB_2O_4 and AB_2O_3, respectively, which indicate that one-half of O_2 should be released by the spinel to yield the rock salt phase (Equation (1)). Maintaining oxygen partial pressure is crucial to get the impurity-free spinel phase.

$$\underset{AB_2O_4}{\text{Spinel structure}} \underset{+1/2O_2}{\overset{-1/2O_2}{\rightleftharpoons}} \underset{AB_2O_3}{\text{Rock salt structure}} \tag{1}$$

A fully reversible spinel to rock salt transformation is driven by a change in oxygen content.[55,56] However, these traces of the rock salt phase can be eliminated by annealing the sample at 700 °C.[48,49] The d-spacing values for P-750 were calculated from the XRD data using Scherrer's equation, and the corresponding data are listed as Table S1, Supporting Information. The d-spacing calculated using XRD match well with high-resolution TEM (HR-TEM) shown in Figure 5. Figure 1b shows the XRD Rietveld refinement data (performed using FullProof software) for the P-750 sample, which shows good agreement between the experimental and calculated data. It confirms the formation of disordered LNMO with the Fd$\bar{3}$m space group with the presence of a small amount of $Li_xNi_{1-x}O$ phase, which is often present in disordered LNMO.
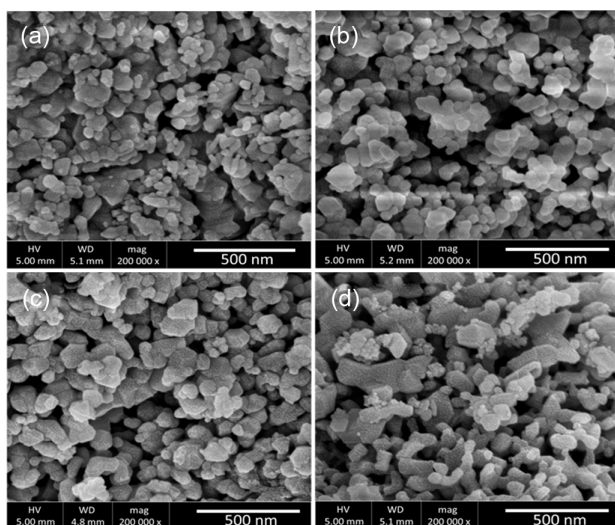
Figure 2. FE-SEM images for a) D-700, b) P-650, c) P-700, and d) P-750 materials.

Figure 2 shows FE-SEM images of the D-700, P-650, P-700, and P-750 samples. It can be seen that the particles have a rock-like morphology with nanometric size. All materials have a particle size ranging from 50 to 150 nm with a well homogeneous particle size distribution as seen in the FE-SEM images. In comparison with P-series materials, D-700 shows a smaller particle size and has particles even smaller than 50 nm in size, as shown in Figure 2a. These smaller particles may be present due to direct calcination of the precursor in microwave sintering without any decomposition step. Under these synthesis conditions, the material did not have sufficient time for particle coarsening; therefore, the particles were smaller. Generally, in conventional sintering, where the dwell time ranges from 8 to 12 h, the particles have enough time for grain coarsening, which results in course and well-crystalline particles. It is also interesting to see that the particles do not show any agglomeration even with small nanometric size, leading to a well-defined rock-like particle morphology.

Table 1 lists the Brunauer–Emmett–Teller (BET) surface area and pore volume of all the synthesized materials. D-700 has the highest surface area of around $18.63 \, m^2 \, g^{-1}$ compared with the materials synthesized after decomposition (the P-series). In contrast, increasing the synthesis temperature decreases the surface area of the materials, which may be due to particle growth and increased grain size. P-750 has a lower surface area, around $8.44 \, m^2 \, g^{-1}$, compared to P-650 and P-700, which have a surface area of 15.20 and $11.27 \, m^2 \, g^{-1}$ respectively.

Table 1. BET surface area and pore volume of synthesized materials.

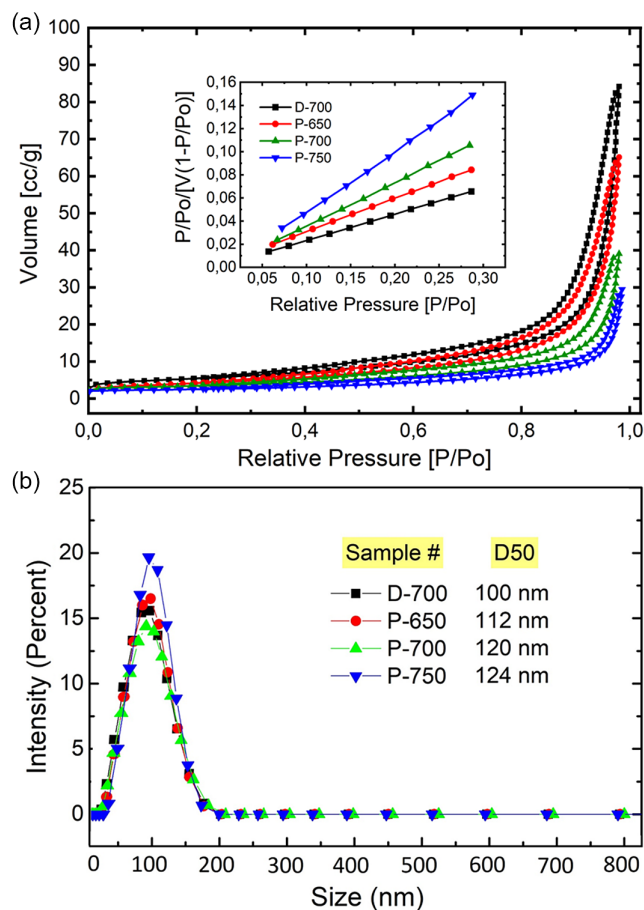| Material	BET surface area [$m^2 \, g^{-1}$]	Pore volume [$cm^3 \, g^{-1}$]
D-700	18.634	0.131
P-650	15.202	0.101
P-700	11.278	0.061
P-750	8.443	0.046

Figure 3. a) N_2 adsorption/desorption isotherms for D-700, P-650, P-700, and P-750 materials; the insert shows the BET plot. b) Particle size distribution for D-700, P-650, P-700, and P-750.

Figure 3a shows the N_2 adsorption/desorption isotherms for the synthesized materials, which correspond to mesoporous-type characteristic behavior. It can be seen from the curves that the D-700 sample shows the highest volume absorption with increase in relative pressures compared to the P-series materials. A material with a higher surface area usually absorbs more gas relative to a material with a lower surface area mainly due to the presence of more active gas adsorption sites. The inset of Figure 3a shows the BET data that were used to calculate the surface area of the materials. Figure 3b shows the particle size distribution for different materials. D50 values calculated using a Zeta Sizer for the D-700, P-650, P700, and P-750 samples are 100, 112, 120, and 124 nm, respectively, as shown in Figure 3b.

TEM analysis was conducted to get more insights into the morphology of prepared materials, as shown in **Figure 4**. As discussed earlier, the material has a very small particle size in the range of ≈50–150 nm. The particles show a rock-like morphology, as shown in Figure 4a–c, which is consistent with our FE-SEM results. Figure 4b,c clearly shows the lattice fringes, which confirm the synthesis of a highly crystalline material even with a small sintering dwell time of 20 min. The lattice spacing is around 0.472 nm, which corresponds to (111) planes of LNMO.
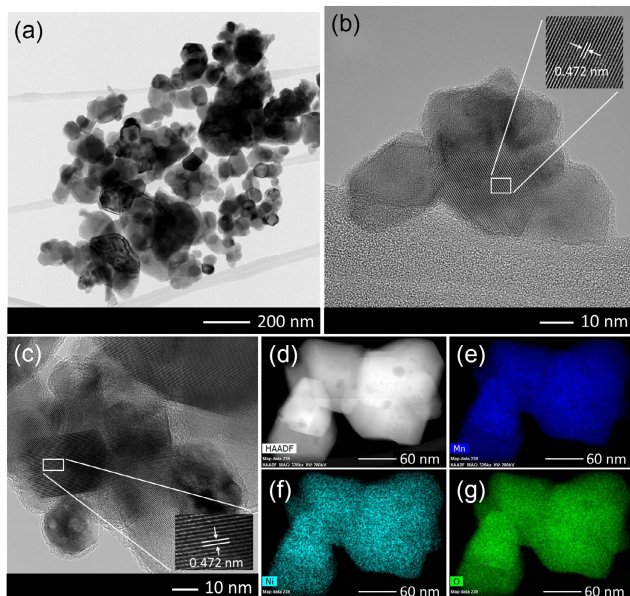
**ADVANCED
SCIENCE NEWS**

www.advancedsciencenews.com

Energy Technology
Generation, Conversion, Storage, Distribution

www.entechnol.de

Figure 4. a–c) TEM and HR-TEM images and d–g) elemental mapping images for P-750.

For more clarity, magnified regions are also included as an inset in Figure 4b,c, which clearly shows the well-defined lattice fringes. Elemental mapping images of P-750 shown in Figure 4d–g confirm the homogenous distribution of Ni, Mn, and O in the synthesized material, which also supports XRD results for the synthesis of pure materials (Figure 1). Generally, if impurity phases are present, they segregate and are not homogeneously distributed throughout the material. Figure S2, Supporting Information, shows the TEM and elemental images for D-700, which also show the homogeneous distribution of Mn, Ni, and O throughout the particles. It is interesting to note that even with a 20 min sintering dwell time, the material demonstrates a well-homogeneous distribution of elements and phase-pure material. The particle size can be found in the range of 20–150 nm, as shown in Figure S2, Supporting Information.

Figure 5a shows the differential capacity (dQ/dV) curves for D-700 and P-750 to compare the involved oxidation and reduction reactions during cycling. The differential capacity (dQ/dV) curve gives information regarding both the underlying thermodynamics and kinetics of the battery systems. But we have used it to reconfirm the presence of disorder phase in both the D-700 and P-750 materials. Both materials show oxidation peaks around 4.03, 4.68, and 4.74 V and reduction peaks around 3.99,
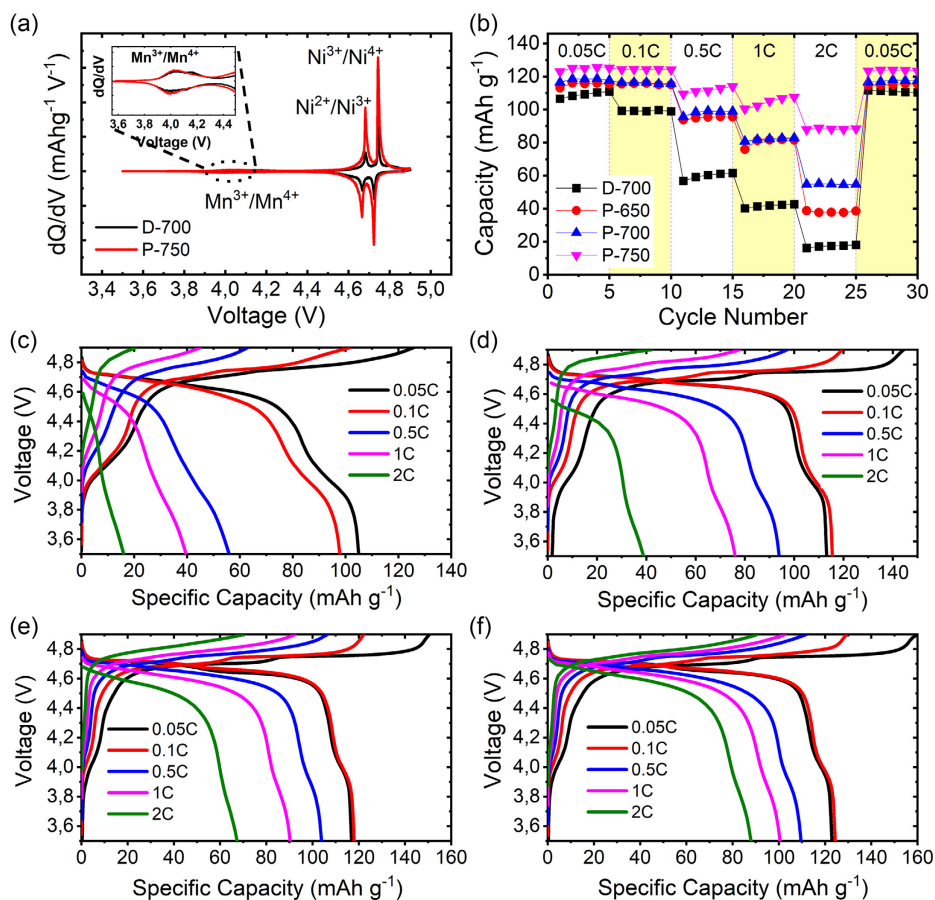

Figure 5. a) dQ/dV curves for D-700 and P-750. b) The discharge capacity of D-700, P-650, P-700, and P-750 at different C-rates (rate capability). c) Charge/discharge curves of D-700, d) P-650, e) P-700, and f) P-750 at different C-rates. The cells are cycled between 3.5 and 4.9 V.

4.64, and 4.72 V, which correspond to Mn^{3+}/Mn^{4+}, Ni^{2+}/Ni^{3+}, and Ni^{3+}/Ni^{4+} redox couples, respectively. The presence of the Mn^{3+}/Mn^{4+} redox couple as clearly seen in the inset in Figure 5a reveals the formation of the disordered phase, which originates from Ni/Mn disordering. It can be observed that the peak intensities for P-750 are quite high compared to D-700, which indicates that the P-750 should exhibit better electronic conductivity compared to D-700. This is considered beneficial in improving the kinetics of this material and thus contributes to demonstrating better electrochemical performance, especially at higher C-rates. Figure 5b shows the rate capability data for D-700, P-650, P-700, and P-750. It can be noted that D-700 shows the lowest initial discharge capacity at all C-rates as well as rapid capacity fading, which may be due to insufficient crystallization time for the material, which affects its electrochemical performance. The discharge capacity at 0.05C is around 110 mA h g^{-1} and decreases rapidly to ≈62 and ≈40 mA h g^{-1} at 0.5C and 1C, respectively. In contrast, P-650, P-700, and P-750 show improved electrochemical performance with higher discharge capacities and improved capacity retention at high C-rates. It should be noted that in these samples, an additional heat treatment step was added to decompose the precursors before final sintering in the microwave furnace during which only the crystallization of materials takes place, contributing to improving the performance. P-650 and P-700 show very similar electrochemical performance with a discharge capacity of around 116 and 80 mA h g^{-1} at 0.05C and 1C, respectively. As a comparison, P-750 shows the best rate capability performance with an initial discharge capacity of around 125 mA h g^{-1} at 0.05, which reduces to 110 and 107 mA h g^{-1} at 0.5C and 1C, respectively. The better rate performance of P-750 may be due to low charge transfer resistance at the electrode/electrolyte interface, high electrical conductivity, and improved ionic diffusivity in this material.

Figure 5c–f shows the galvanostatic charge/discharge behavior of all the synthesized materials at different C-rates. It can be observed from Figure 5c that D-700 shows a discharge capacity of ≈107 and 19 mA h g^{-1} at 0.05C and 2C, respectively. This indicates that there is rapid capacity fading in this material with increasing C-rate. In contrast, P-650, P-700, and P-750 demonstrate improved discharge capacities and higher capacity retention at high C-rates, as shown in Figure 5d–f. As a comparison, P-750 shows the best rate performance in terms of initial discharge capacity (125 mA h g^{-1} at 0.05C) and capacity retention (90 mA h g^{-1} at 2C). It is pertinent to note that P-650, P-700, and P-750 have a lower amount of disorder compared to D-700 as clearly shown in the galvanostatic charge/discharge curves in Figure 5c–f which correspond to the Mn^{3+}/Mn^{4+} redox couple at around 4.0 V. The improved performance of these materials, particularly of P-750, when compared to D-700, may be due to the better electronic conductivity of the material as also evident in dQ/dV in Figure 5a. Also, the increased crystallinity of the materials synthesized at a higher temperature may have contributed to the improvement of the material's ionic conductivity, resulting in improved electrochemical performance. As P-750 displays the best rate capability performance, we calculated the Li-ion diffusion coefficient of the P-750 sample using cyclic voltammetry (CV) and the Randles–Sevcik equation. The calculated diffusion coefficient is 6.625×10^{-11} cm^2 s^{-1}, which is consistent with the previous literature.[57] The CV curve for P-750 is shown in Figure S3, Supporting Information.

Figure 6a shows the cycling performance of D-700, P-650, P-700, and P-750 at 0.05C for 50 cycles. As shown in Figure 6, the initial discharge capacity of P-650, P-700, and P-750 is higher when compared to D-700. P-750 shows the highest discharge capacity of around 122 and 119.99 mA h g^{-1} at 0.05C and 0.1, respectively, when compared to D-700, which shows a capacity of around 110 and 101.44 mA h g^{-1}. Comparison with D-700, the greater initial capacities of P-650, P-700, and P-750 could be directly related to their improved electrical conductivity and ionic diffusivity. P-650 shows faster capacity fading at both 0.05C and 0.1C, whereas the other materials show very slow capacity fading, as shown in Figure 6a,b. The capacity fading in P-650 may also be due to the low sintering temperature resulting in low crystallinity in the material structure, which hinders the ionic movement and results in poor performance. Generally, in conventional sintering, 900 °C is the ideal temperature to synthesize LNMO for good electrochemical performance. Lower sintering temperatures usually do not give the best performance.[27,58,59] In contrast, P-750 not only shows the highest discharge capacity but also shows the best capacity retention of around 96.36% and 93.85% at 0.05C and 0.1C after 50 and 100 cycles, respectively. As discussed before, the better electrochemical performance of P-750 may be due to the low charge transfer resistance at the electrode/electrolyte interface, high electrical conductivity, and improved ionic diffusivity in this material.

Figure 6c–f displays the galvanostatic charge/discharge profiles of different samples after the 1st, 10th, 20th, 30th, 40th, and 50th cycle when cycled at 0.05C. The cells were charged/discharged between 3.5 and 4.9 V. All the samples exhibit high (4.7 V) and low (4.0 V) voltage plateaus, which are present in disordered spinel LNMO. It can be observed that the voltage profiles are slightly different from each other. The difference lies in the lower-voltage plateaus at around 4.0 V, which correspond to the Mn^{3+}/Mn^{4+} redox couple. All the samples have different amounts of the Ni/Mn disorder (calculated on the basis of the ratio of the capacity delivered by the high-voltage and lower-voltage plateau) as highlighted in yellow (1st cycle comparison) in Figure 6c–f, which may originate from the difference in synthesis temperature conditions. The ordered and disordered phases of LNMO are defined by the distribution of Ni and Mn in the crystal structure. In the ordered phase, Ni and Mn are distributed 1:3, where all the Mn is in the Mn^{4+} valent state, whereas in the disordered phase Ni and Mn are distributed randomly, and some of the Mn exist as the Mn^{3+} state and the amount of Mn^{3+} is proportional to the degree of the disordered phase. Therefore, the ratio of the capacity delivered by the high-voltage (4.7 V) and low-voltage (4.0 V) plateaus can provide the estimation of the degree of Ni/Mn disorder. The more is the capacity delivered by the lower-voltage plateaus, the higher is the Ni/Mn disordered. This can give a good estimate (qualitatively) of the amount of disorder in high-voltage spinel LNMO. As mentioned earlier, P-650 shows faster voltage decay compared to the other materials shown in Figure 6d, which may be due to the lower synthesis temperature. It is also noted that P-750 not only shows excellent capacity retention but also has a lesser amount of Ni/Mn disorder, as shown in Figure 6f. Figure S4, Supporting Information, shows the galvanostatic
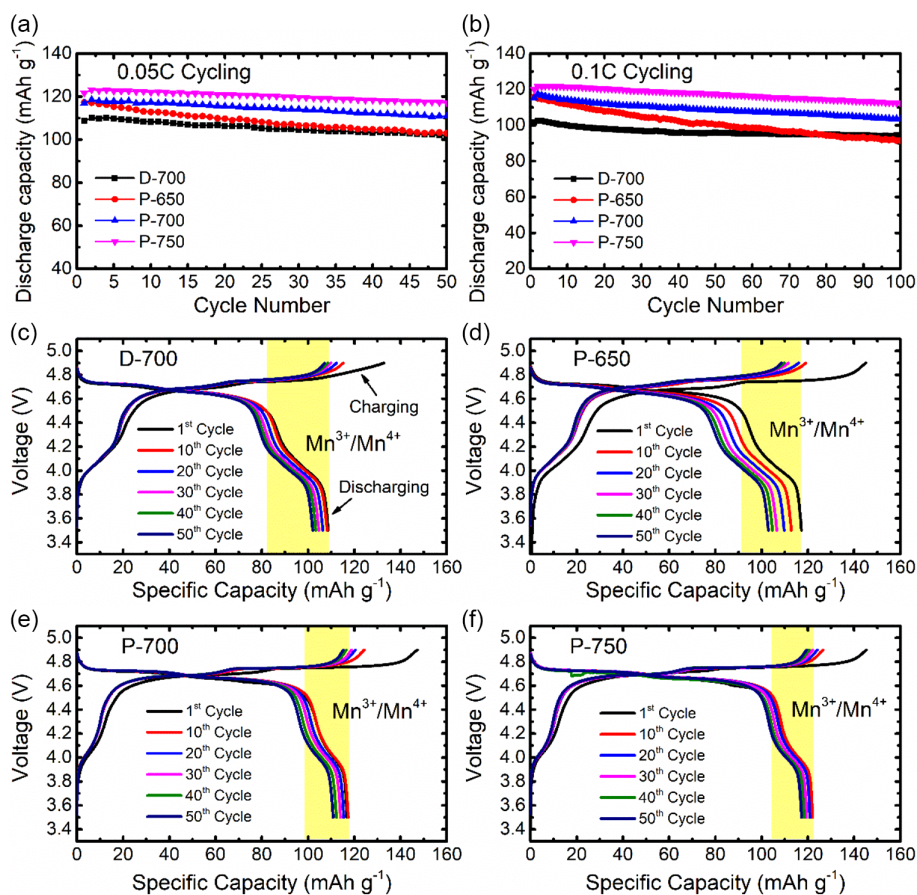
ADVANCED
SCIENCE NEWS
www.advancedsciencenews.com

Energy Technology
Generation, Conversion, Storage, Distribution
www.entechnol.de

Figure 6. Cycling behavior of D-700, P-650, P-700, and P-750 at a) 0.05C and b) 0.1C for 50 cycles. c–f) Charge/discharge profiles of D-700, P-650, P-700, and P-750 after 1st, 10th, 20th, 30th, 40th, and 50th cycles at 0.05C. The cells are cycled between 3.5 and 4.9 V.

charge/discharge profiles of different samples after the 1st, 20th, 40th, 60th, 80th, and 100th cycle when cycled at 0.1C. The voltage profiles for all the materials are very similar to when they are cycled at 0.05C. P-650 shows rapid capacity fading, as shown in Figure S-4b, Supporting Information, whereas all the other materials show relatively stable cycling. Furthermore, the amount of disorder in D-700 and P-650 is more when compared to P-700 and P-750, which may be due to the difference in heat treatment temperatures.

Table 2 shows the degree of Ni/Mn disorder in various materials, which is roughly between 14% and 24%. The degree of Ni/Mn disorder is calculated based on the ratio of the capacity

Table 2. The amount of Ni/Mn disorder in different materials. The Ni/Mn disorder is calculated approximately based on the capacity delivered by the first cycle at the 4.0 V plateau (Mn^{3+}/Mn^{4+} redox couple).

Material	Amount of Ni/Mn disorder [%]
D-700	23.54
P-650	20.27
P-700	15.05
P-750	14.33

delivered by the high voltage (4.7 V) and lower voltage (3.0 V) during the first cycle, as highlighted in yellow in Figure 6c–f. It is observed that the materials synthesized with pre-heat treatment step (P-650, P-700, and P-750) have a lesser degree of Ni/Mn disorder compared with the material synthesized without a pre-heat treatment step (D-700). Moreover, the Ni/Mn disorder decreases with the increase in heat treatment temperature. P-750 shows the least amount of Ni/Mn disorder of around 14.33%, which can also be well observed in galvanostatic curves in Figure 6c–f.

EIS measurements were recorded during the first cycle at different potentials during the charging/discharging states, as shown in **Figure 7**. The symbol represents the experimental data points, and the fitted data are represented as continuous black lines in the P-750 samples. The obtained data were analyzed by fitting with an electrical equivalent circuit (Figure S5, Supporting Information) consisting of electrolyte resistance (R1: R_e), the electronic resistance (R2: R_{sf}) of the individual active particle, charge transfer (R3: R_{ct}) resistance at the electrode/electrolyte interface and bulk resistances (R4: R_b), as well as capacitances, constant phase elements (C2, CPE3, and C4), and the finite Warburg impedance (W_o). The Z-view software was used for experimental data fitting within the frequencies regime. Figure 7c shows the resistances R1, R2, and R3 are
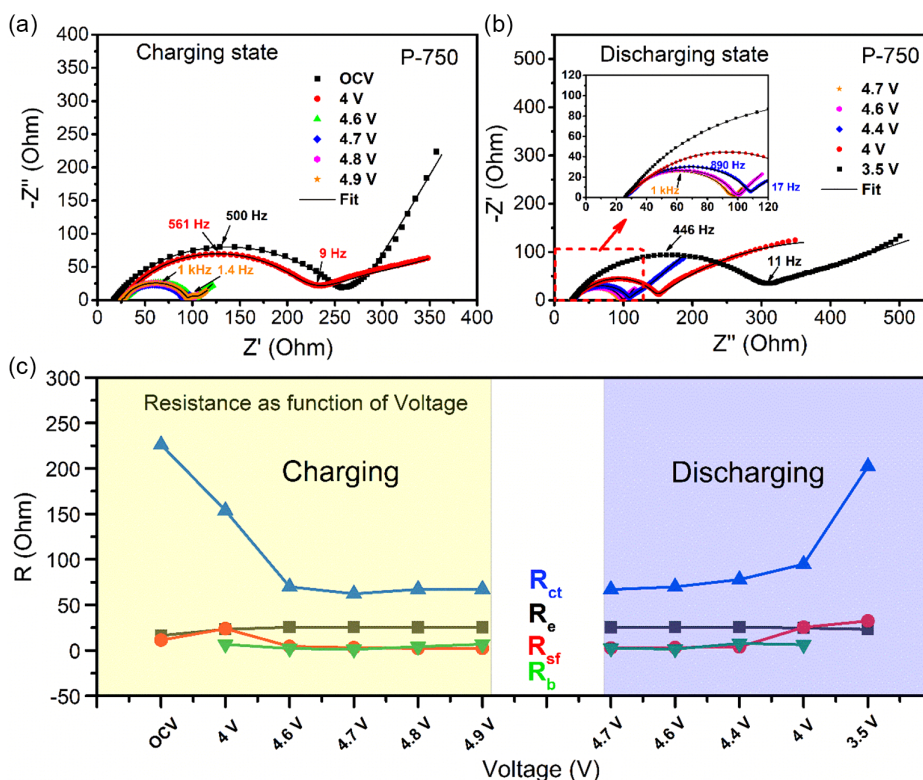
Figure 7. EIS spectra during the first cycle at different potentials during a) charging and b) discharging states and c) resistances R_e, R_{sf}, R_{ct}, and R_{dl} shown as a function of the voltage during the charge–discharge cycle for the P-750 sample.

displaying as a function of the voltage during the charge–discharge cycle of P-750 samples. The Ohmic electrolyte resistance R_e values are constant regardless of the material and voltage during the charge/discharge cycle, which is an indication of stable ionic resistivity of the used electrolyte. In the charging state, the value of electronic resistance of the cathode particle (R_{sf}) are not changing at open circuit voltage and 4 V; after that, the R_{sf} values decrease and are stable until 4.9 V (fully charged state). After 4 V, the electronic conductivity increases with increasing Mn^{4+} content. The interfacial charge transfer resistance (R_{ct}) decreases till 4.6 V and after that R_{ct} values are stable until 4.9 V. This might be due to the effect of nickel oxidation from 2^+ to 3^+ on particle conductivity and charge transfer. R_{dl} is the impedance response of a single intercalation particle that is surrounded by a resistance film and the values are almost stable during the charge/discharge cycle.[60–62] In discharging, the R_{sf} and R_{ct} value are stable up to 4.4 V, then increasing to the end of the discharge cycle. The electronic conductivity and charge transfer are decreasing with increasing Ni^{2+} content in the active material. From this discussion, it is confirmed that the electronic conductivity is most important for the charge transfer mechanism at the electrode/electrolyte interface.

3. Conclusion

Novel fast and cost-effective synthesis of high-voltage spinel LNMO is undertaken using sol–gel synthesis followed by a

microwave sintering approach. Structural analysis (XRD, FE-SEM, HR-TEM) confirms the formation of nanocrystalline (50–150 nm), phase-pure materials having a rock-like morphology exhibiting a homogeneous distribution of manganese, nickel, and oxygen within the particles without any segregation. The material synthesized at 750 °C (P-750) shows the best electrochemical performance (high discharge capacity, good cyclability, and improved rate capability) compared to the other developed materials. The improved electrochemical performance of P-750 may be attributed to better crystallinity at higher synthesis temperature, its low charge transfer resistance at the electrode/electrolyte interface, high electrical conductivity, and improved ionic diffusivity. If properly engineered, microwave sintering may play an important role in the cost-effective production of electrode materials for lithium-ion batteries, contributing to reducing the battery cost.

4. Experimental Section

Material Preparation: The materials were synthesized using a sol-gel assisted microwave synthesis approach. First, 100 mL of deionized (DI) water was heated in a glass beaker at 60 °C with continuous stirring. Then lithium, nickel, and manganese acetate (Sigma Aldrich) were added to the DI water and left for 30 min until they dissolved completely. Later, citric acid (Sigma Aldrich, ACS reagent ≥99.5%, metal ions to citric acid 1:1) was added to the precursor solution as a chelating agent. The temperature of the solution was then increased to 80 °C with continuous stirring for 12 h to completely dry the precursor solution. Once all the

DI water was evaporated, the precursor mixer was ground and homogeneously mixed using agate mortar. The powder was then pressed into small pellets using a stainless steel die of 10 mm diameter for sintering. For a complete comparison purpose, the materials were prepared into two batches. In the first batch, the prepared precursor pellets were directly transferred to the microwave furnace and sintered in air at 700 °C for 20 min (named "D-700"). For the other batch, the precursors were first preheated at around 450 °C for 6 h in the air in a conventional furnace to decompose the precursors. Later, these decomposed precursors were reground, pressed into pellets, and finally sintered in the microwave furnace at 650, 700, and 750 °C for 20 min (named "P-650," "P-700," and "P-750") in air. The heat treatment at 450 °C ensures complete decomposition of the precursors and facilitates achieving improved crystallinity and stable crystal structure of materials during the subsequent microwave sintering step.

Structural, Compositional, and Physical Characterization: Powder XRD measurements were performed to identify the phase purity of all the synthesized materials using a PANalytical diffractometer (Empyrean) equipped with Cu Kα radiation. The XRD patterns were collected between $10° \leq 2\theta \leq 90°$ with the step size of 0.01°. The particle morphology (shape, size, and distribution) was investigated using FE-SEM (Nova). To prepare the samples for SEM analysis, a small amount of powder (LNMO) was spread on the carbon tape attached on the top of the aluminum stub which was gold sputtered for 40 s. Furthermore, a transmission electron microscope (Talos F200X, FEI) was used to take elemental mapping and high-resolution images of the prepared materials. The TEM samples were prepared by dispersing the powder sample in ethanol and sonicated for 10 min to get a well-dispersed material. Later, this material was dispersed on a copper grid and dried in an oven at 80 °C for 15 min. TGA (Perkin Elmer, TGA 4000) was performed for the precursor LNMO material from room temperature to 700 °C at the heating rate of 10 °C. The BET surface area of the samples was measured using an AimSizer (AS-3012). Finally, the particle size distribution of the materials was measured using a Malvern Zeta Sizer (Nano ZSP).

Electrode Fabrication: The cathode for the electrochemical testing was fabricated by making a slurry of active material (LNMO), conductive carbon (Super-P), and polyvinylidene fluoride (PVDF) in 1-methyl-2-pyrrolidone (NMP) as a solvent. The ratio of active material, carbon, and PVDF was 80:10:10 (wt%). The slurry was allowed to mix in a glass vial for ≈6 h to get homogenous mixing of all the materials. The slurry was then cast on aluminum foil, using a doctor blade technique. The cast electrode was immediately shifted to the oven at 120 °C and dried for 2 h to remove the NMP solvent. The dried electrode was then calendared using a rolling press. Electrodes with a diameter of 14 mm were punched from this calendared electrode, which were then shifted to a vacuum oven operating at 120 °C to remove the traces of moisture. Finally, the dried electrodes were shifted to a glove box for cell assembly.

Electrochemical Measurements: Electrochemical measurements were conducted using a 2032-type coin cell assembled in an argon-filled glove box. Lithium metal, synthesized LNMO materials, and Celgard 2325 were used as the anode, cathode, and separator, respectively. The electrolyte was composed of 1 M LiPF$_6$ in a mixture of dimethyl carbonate (DMC) and ethylene carbonate (EC) (1:1 by v/v) (Sigma Aldrich). Electrochemical measurements were performed in the voltage window of 3.5–4.9 V using a WonAtech WBCS 3000L battery cycler. Electrochemical impedance measurements (EIS) were performed using a Solartron battery cycler (1470E). For the EIS analysis, the two-electrode system (Li-ion half-cell configuration) was used with lithium metal as the anode and reference electrode, and the synthesized LNMO materials as the working electrode (cathode).

Conflict of Interest

The authors declare no conflict of interest.

Data Availability Statement

The data that support the findings of this study are available from the corresponding authors upon reasonable request.

[1] M. Armand, J.-M. Tarascon, *Nature* **2008**, *451*, 652.
[2] J.-M. Tarascon, *Philos. Trans. R. Soc., A* **2010**, *368*, 3227.
[3] D. Larcher, J.-M. Tarascon, *Nat. Chem.* **2015**, *7*, 19.
[4] G. Jeong, Y.-U. Kim, H. Kim, Y.-J. Kim, H.-J. Sohn, *Energy Environ. Sci.* **2011**, *4*, 1986.
[5] N. Nitta, F. Wu, J. T. Lee, G. Yushin, *Mater. Today* **2015**, *18*, 252.
[6] M. Armand, J.-M. Tarascon, *Nature* **2008**, *451*, 652.
[7] C. M. Julien, A. Mauger, *Ionics* **2013**, *19*, 951.
[8] U. Nisar, R. Amin, R. Essehli, R. A. Shakoor, R. Kahraman, D. K. Kim, M. A. Khaleel, I. Belharouak, *J. Power Sources* **2018**, *396*, 774.
[9] M. Jo, M. Noh, P. Oh, Y. Kim, J. Cho, *Adv. Energy Mater.* **2014**, *4*, 1.
[10] W. Liu, G. Hu, K. Du, Z. Peng, Y. Cao, *J. Power Sources* **2013**, *230*, 201.
[11] P. R. Kumar, A. Kheireddine, U. Nisar, R. A. Shakoor, R. Essehli, R. Amin, I. Belharouak, *J. Power Sources* **2019**, *429*, 149.
[12] P. Ge, S. Li, L. Xu, K. Zou, X. Gao, X. Cao, G. Zou, H. Hou, X. Ji, *Adv. Energy Mater.* **2019**, *9*, 180303.
[13] U. Nisar, S. A. J. A. Al-Hail, R. K. Petla, R. A. Shakoor, R. Essehli, R. Kahraman, S. Y. AlQaradawi, D. K. Kim, I. Belharouak, M. R. Amin, *Energy Mater.* **2019**, *2*, 7263.
[14] Y. Wei, K. Tuo, P. Wang, L. Yang, W. Liang, H. Ding, X. Cui, S. Li, *Ionics* **2020**, *26*, 6003.
[15] H. Q. Wang, F. Y. Lai, Y. Li, X. H. Zhang, Y. G. Huang, S. J. Hu, Q. Y. Li, *Electrochim. Acta* **2015**, *177*, 290.
[16] D. Wang, X. Li, Z. Wang, H. Guo, Y. Xu, Y. Fan, J. Ru, *Electrochim. Acta* **2016**, *188*, 48.
[17] H. Bang, D.-H. Kim, Y. C. Bae, J. Prakash, Y.-K. Sun, *J. Electrochem. Soc.* **2008**, *155*, A952.
[18] S. M. Bak, E. Hu, Y. Zhou, X. Yu, S. D. Senanayake, S. J. Cho, K. B. Kim, K. Y. Chung, X. Q. Yang, K. W. Nam, *ACS Appl. Mater. Interfaces* **2014**, *6*, 22594.
[19] H. Konishi, M. Yoshikawa, T. Hirano, *J. Power Sources* **2013**, *244*, 23.
[20] S.-K. Jung, H. Gwon, J. Hong, K.-Y. Park, D.-H. Seo, H. Kim, J. Hyun, W. Yang, K. Kang, *Adv. Energy Mater.* **2014**, *4*, 1300787.
[21] U. Nisar, R. Petla, S. A. J. Al-hail, A. A. Quddus, H. Monawwar, A. Shakoor, R. Essehli, R. Amin, *RSC Adv.* **2020**, *10*, 15274.

[22] C. X. Ding, Y. C. Bai, X. Y. Feng, C. H. Chen, *Solid State Ionics* **2011**, *189*, 69.

[23] Y. Cho, Y. S. Lee, S. A. Park, Y. Lee, J. Cho, *Electrochim. Acta* **2010**, *56*, 333.

[24] L. X. Yuan, Z. H. Wang, W. X. Zhang, X. L. Hu, J. T. Chen, Y. H. Huang, J. B. Goodenough, *Energy Environ. Sci.* **2011**, *4*, 269.

[25] W. Liang, P. Wang, B. Wang, H. Ding, S. Li, *J. Mater.* **2021**.

[26] D. Zhao, J. Wang, H. Lu, P. Wang, H. Liu, S. Li, *J. Power Sources* **2020**, *456*, 228006.

[27] H. Liu, J. Wang, X. Zhang, D. Zhou, X. Qi, B. Qiu, J. Fang, R. Kloepsch, G. Schumacher, Z. Liu, J. Li, *ACS Appl. Mater. Interfaces* **2016**, *8*, 4661.

[28] T. Q. Tan, S. P. Soo, A. Rahmat, J. B. Shamsul, R. A. M. Osman, Z. Jamal, M. S. Idris, *Adv. Mater. Res.* **2013**, *795*, 245.

[29] Y. K. Sun, D. J. Lee, Y. J. Lee, Z. Chen, S. T. Myung, *ACS Appl. Mater. Interfaces* **2013**, *5*, 11434.

[30] U. Nisar, R. Amin, A. Shakoor, R. Essehli, S. Al-Qaradawi, R. Kahraman, I. Belharouak, *Emergent Mater.* **2018**, *1*, 155.

[31] X. Liu, P. He, H. Li, M. Ishida, H. Zhou, *J. Alloys Compd.* **2012**, *552*, 76.

[32] H. Guo, Z. Wei, K. Jia, B. Qiu, C. Yin, F. Meng, Q. Zhang, L. Gu, S. Han, Y. Liu, H. Zhao, W. Jiang, H. Cui, Y. Xia, Z. Liu, *Energy Storage Mater.* **2019**, *16*, 220.

[33] W. Xu, Y. Zhou, X. Ji, *J. Phys. Chem. Lett.* **2018**, *9*, 4976.

[34] S. Yang, D. O. Schmidt, A. Khetan, F. Schrader, S. Jakobi, M. Homberger, M. Noyong, A. Paulus, H. Kungl, R. A. Eichel, H. Pitsch, U. Simon, *Materials* **2018**, *11*, 1.

[35] Y. Cho, S. Lee, Y. Lee, T. Hong, J. Cho, *Batteries* **2011**, *15*, 821.

[36] M.-H. Lee, Y.-J. Kang, S.-T. Myung, Y.-K. Sun, *Electrochim. Acta* **2004**, *50*, 939.

[37] E. Han, Q. Jing, L. Zhu, G. Zhang, S. Ma, *J. Alloys Compd.* **2015**, *618*, 629.

[38] H.-W. Lee, P. Muralidharan, C. M. Mari, R. Ruffo, D. K. Kim, *J. Power Sources* **2011**, *196*, 10712.

[39] H. W. Lee, P. Muralidharan, R. Ruffo, C. M. Mari, Y. Cui, D. K. Kim, *Nano Lett.* **2010**, *10*, 3852.

[40] Q. Xie, C. Zhao, Z. Hu, Q. Huang, C. Chen, K. Liu, *RSC Adv.* **2015**, *5*, 77324.

[41] D. Wang, I. Belharouak, G. M. Koenig, G. Zhou, K. Amine, *J. Mater. Chem.* **2011**, *21*, 9290.

[42] M. Zhang, Y. Liu, Y. Xia, B. Qiu, J. Wang, Z. Liu, *J. Alloys Compd.* **2014**, *598*, 73.

[43] D. Wang, I. Belharouak, G. Zhou, K. Amine, *J. Electrochem. Soc.* **2013**, *160*, A3108.

[44] W. Liu, P. Gao, Y. Mi, J. Chen, H. Zhou, X. Zhang, *J. Mater. Chem. A* **2013**, *1*, 2411.

[45] I. Veljkovic, D. Poleti, L. Karanovic, M. Zdujic, G. Brankovic, *Sci. Sinter.* **2011**, *43*, 343.

[46] U. Nisar, M. H. Gulied, R. A. Shakoor, R. Essehli, Z. Ahmad, A. Alashraf, R. Kahraman, S. Al-Qaradawi, A. Soliman, *RSC Adv.* **2018**, *8*, 32985.

[47] M. A. Kebede, S. N. Yannopoulos, L. Sygellou, K. I. Ozoemena, *J. Electrochem. Soc.* **2017**, *164*, 3259.

[48] S. Shi, S. Zhang, Z. Wu, T. Wang, J. Zong, M. Zhao, G. Yang, *J. Power Sources* **2017**, *337*, 82.

[49] G. Yang, G. Wang, W. Hou, *J. Phys. Chem. B* **2005**, *109*, 11186.

[50] H. Hua, L. Han-xing, O. Shi-xi, *J. Wuhan Univ. Technol. Sci. Ed.* **2008**, *17*, 36.

[51] Z. Dong Peng, Y. Bing Cao, G. Rong Hu, K. Du, X. Guang Gao, Z. Wei Xiao, *Chem. Lett.* **2009**, *20*, 1000.

[52] K.-S. Lee, S.-T. Myung, Y.-K. Sun, *Chem. Mater.* **2007**, *19*, 2727.

[53] P. Gao, L. Wang, L. Chen, X. Jiang, J. Pinto, G. Yang, *Electrochim. Acta* **2013**, *100*, 125.

[54] L. S. Lobo, A. R. Kumar, *J. Sol-Gel Sci. Technol.* **2016**, *80*, 821.

[55] N. Reeves-McLaren, J. Sharp, H. Beltrán-Mir, W. M. Rainforth, A. R. West, *Proc. R. Soc. A Math. Phys. Eng. Sci.* **2016**, *472*, 20140991.

[56] N. Reeves, C. A. Kirk, A. R. West, *J. Mater. Chem.* **2001**, *11*, 249.

[57] W. Liu, Q. Shi, Q. Qu, T. Gao, G. Zhu, J. Shao, H. Zheng, *J. Mater. Chem. A* **2017**, *5*, 145.

[58] J. Ma, P. Hu, G. Cui, L. Chen, *Chem. Mater.* **2016**, *28*, 3578.

[59] B. J. Hwang, Y. W. Wu, M. Venkateswarlu, M. Y. Cheng, R. Santhanam, *J. Power Sources* **2009**, *193*, 828.

[60] R. Amin, I. Belharouak, *J. Power Sources* **2017**, *348*, 311.

[61] R. Amin, I. Belharouak, *J. Power Sources* **2017**, *348*, 318.

[62] I. Particles, J. P. Meyers, M. Doyle, R. M. Darling, J. Newman, *J. Electrochem. Soc.* **2000**, *147*, 2930.